

RESEARCH

Open Access



Biosynthesis, characterization and optimization of TiO₂ nanoparticles by novel marine halophilic *Halomonas* sp. RAM2: application of natural dye-sensitized solar cells

Rasha A. Metwally^{1*}, Jehan El Nady², Shaker Ebrahim³, Amany El Sikaily⁴, Nermeen A. El-Sersy¹, Soraya A. Sabry⁵ and Hanan A. Ghozlan⁵

Abstract

Background Metal oxide nanoparticles (NPs) are becoming valuable due to their novel applications. The green synthesis of TiO₂ NPs is more popular as a flexible and eco-friendly method compared to traditional chemical synthesis methods. TiO₂ NPs are the most commonly used semiconductor in dye-sensitized solar cells (DSSCs).

Results The biogenic TiO₂ NPs were produced extracellularly by the marine halophilic bacterium *Halomonas* sp. RAM2. Response surface methodology (RSM) was used to optimize the biosynthesis process, resulting in a starting TiO₂ concentration of 0.031 M and a pH of 5 for 92 min (~15 nm). TiO₂ NPs were well-characterized after the calcination process at different temperatures of 500, 600, 700 and 800 °C. Anatase TiO₂ NPs (calcined at 500 °C) with a smaller surface area and a wider bandgap were nominated for use in natural dye-sensitized solar cells (NDSSCs). The natural dye used as a photosensitizer is a mixture of three carotenoids extracted from the marine bacterium *Kocuria* sp. RAM1. NDSSCs were evaluated under standard illumination. After optimization of the counter electrode, NDSSC_{Bio(10)} (10 layers) demonstrated the highest photoelectric conversion efficiency (η) of 0.44%, which was almost as good as NDSSC_{P25} (0.55%).

Conclusion The obtained results confirmed the successful green synthesis of TiO₂ NPs and suggested a novel use in combination with bacterial carotenoids in DSSC fabrication, which represents an initial step for further efficiency enhancement studies.

Keywords TiO₂ nanoparticles, Carotenoids, Dye-sensitized solar cells, *Halomonas*, *Kocuria*, Bacterioruberins, Spirilloxanthin

Background

Nanotechnology has profoundly transformed science and plays a worthy role in several innovative aspects of the new millennium. Particularly in comparison to bulk materials, NPs have distinct physical, chemical, and biological properties. It is widely assumed that the basic properties of nanostructured materials are mediated by their sizes and shapes. As a consequence, hard

*Correspondence:

Rasha A. Metwally

rashaabdou2012@hotmail.com; RashaMetwally@alexu.edu.eg

Full list of author information is available at the end of the article



© The Author(s) 2023. **Open Access** This article is licensed under a Creative Commons Attribution 4.0 International License, which permits use, sharing, adaptation, distribution and reproduction in any medium or format, as long as you give appropriate credit to the original author(s) and the source, provide a link to the Creative Commons licence, and indicate if changes were made. The images or other third party material in this article are included in the article's Creative Commons licence, unless indicated otherwise in a credit line to the material. If material is not included in the article's Creative Commons licence and your intended use is not permitted by statutory regulation or exceeds the permitted use, you will need to obtain permission directly from the copyright holder. To view a copy of this licence, visit <http://creativecommons.org/licenses/by/4.0/>. The Creative Commons Public Domain Dedication waiver (<http://creativecommons.org/publicdomain/zero/1.0/>) applies to the data made available in this article, unless otherwise stated in a credit line to the data.

investigations have been made to control the appropriate morphologies of these nanostructure materials [1].

Metal oxide nanoparticles constitute one of the most multi-functional and ubiquitously used types, with applications in electronics, chemistry, catalysts, and medical and pharmaceutical disciplines [2]. Among them are titanium dioxide nanoparticles (TiO_2 NPs), which have become a great addition to nanotechnology due to their tremendous applications as photocatalysts and UV absorbers [3, 4].

Chemical, physical, and biological processes can all be used to construct crystalline TiO_2 nanoparticles with distinct morphologies [5]. Regrettably, toxic chemicals and time-consuming procedures in traditional synthesis techniques frequently endanger humans and the environment. Biosynthesized nanoparticles are eco-friendly and safe, and have been incorporated into various successful and efficient applications as reported in many studies. The biosynthesis of TiO_2 NPs using microorganisms is an alternative green route to overcome these disadvantages while maintaining their excellent properties [6]. During the biological synthesis of NPs, microbial metabolites including enzymes, terpenoids, and phenolics act as stabilizers and capping agents [7]. A major field of interest is the advantage of flexibility in monitoring the experimental conditions of nanoparticle microbial synthesis, such as pH and temperature, which influence the physicochemical characteristics such as morphology, stability, and properties of the biosynthesized nanoparticles [8].

Although green synthesis of nanoparticles is a part of bioinspired protocols, several challenges should be considered. Material availability, selection, collection, reaction conditions, quality management and application face challenges for large-scale applications in industry [9]. Both the size and shape of NPs are highly influenced by the prepared biological extracts. As a result, it is critical to find the ideal conditions and components in order to implement and optimize the synthesis protocol for the purpose of getting NPs with the required size, shape, and surface charges [10]. Green and nontoxic reducing agents were an important question in the green synthesis of NPs, as they are weak to form high-quality NPs. Thus, researchers seek to find stronger green reducing agents or optimum reaction conditions that support the formation of the desired high-quality NPs; this continues to be a tricky and critical challenge [11]. NPs face characterization challenges, which have a major impact on the accuracy of the detailed characterization, as deciding on an appropriate characterization technique is thus critical [12].

Analytical techniques such as transmission electron microscopy (TEM), selected area electron diffraction (SAED), energy dispersive X-ray (EDX), X-ray diffraction

(XRD), UV–visible spectroscopy, and Brunauer-Emmett and Teller (BET) surface area can be used to explore important characters such as the size, phase, surface area and band gap of the synthesized TiO_2 NPs [13].

Recently, researchers concluded that marine bacteria, particularly the halophilic ones, are valuable and unique sources of bioactive compounds and have enzymatic activities with properties distinct from those of conventional enzymes [14]. So, in this study, the green TiO_2 NPs synthesis was selected by using the marine halophilic bacteria *Halomonas* sp. RAM2 via the extracellular route.

Solar energy offers an environmentally friendly alternative to meet the world's growing energy demand. Hence, photovoltaic devices that help in the conversion of solar energy into electricity have gained a great deal of attention recently [15]. DSSCs have sparked impressive attention for their structure simplicity, relatively low cost, and encouraging efficiency in transforming solar energy into electricity [16]. O'Regan and Grätzel pioneered this technology in 1991 [17].

TiO_2 is an important photocatalytic material in DSSCs that exists in two main phases: anatase and rutile [18]. Although rutile seems to be the most thermodynamically stable phase, anatase is chosen due to its larger band gap for DSSCs [19]. TiO_2 is commonly used as a semiconducting layer due to its non-toxicity, low cost, and wide availability [20]. Improving functionalities in solar cells are influenced by the size of nanocrystals during a solid–solid phase transition. So, phase control is a critical step [21].

In general, DSSCs are assembled from the photoanode (working electrode), which is mainly a conductive transparent substrate (fluorine-doped tin oxide (FTO) glass), with the use of an overlying semiconductor film such as TiO_2 that adsorbs the photosensitizer dye, providing the photoelectrons [22]. The working electrode is coupled with the counter electrode that serves as a reduction catalyst. In between, an electrolyte that functions as a redox couple is injected [20, 23].

Photosensitizers are among the most key parts of DSSC and have been extensively studied in the last 20 years, with thousands of dyes suggested and evaluated for this type of application [24]. Till now, DSSCs have been based on a single sensitizer such as ruthenium or porphyrin dyes, which have some limitations such as rareness, purification difficulties and environmental hazards [25]. So, renewable, eco-friendly, and non-carcinogenic natural dyes have attracted attention as photosensitizers [26].

One of the natural pigments is carotenoids, which come in various colors, ranging from yellow to orange and red. Over 750 carotenoids have been observed in plants, fungi, and microorganisms with a wide range of significant biological functions, including light-harvesting,

photoprotection and antioxidants [27, 28]. They are classified as C_{30} , C_{40} , C_{42} or C_{50} based on the number of carbons in their carotene backbones [29]. As an example of the uncommon carotenoids used in the present study, those that were extracted from the marine bacterium *Kocuria* sp. RAM1. *Kocuria* sp. RAM1 dye is a mixture of three carotenoid compounds, namely bisanhydrobacterioruberin, trisanhydrobacterioruberin (C_{50} -carotenoids) and 3,4,3',4'-tetrahydrospirilloxanthin (C_{42} -carotenoids) [30].

The counter electrode plays a role in collecting and transferring electrons from the external circuit and regenerates the dye by catalyzing electrolyte reduction. Pt-coated FTO is widely used as a counter electrode, but there is an interest in replacing it due to its high cost [31]. One alternative to the Pt counter electrode is the Cu_2S counter electrode, which has good performance for polysulfide electrolytes at a low cost. In addition, Cu_2S counter electrodes can be simply prepared by the successive ionic layer adsorption and reaction (SILAR) technique, which controls the film microtopography through changing deposition times [32].

The basic component in DSSCs is the electrolyte, which is critical for the inner charge carrier transport between the two electrodes and regenerates the dye and itself continuously, thus significantly impacting the efficiency and stability of the systems [32, 33]. Several studies reported the use of various redox couples of electrolytes other than I^-/I^{3-} to enhance the durability of DSSCs, such as the redox couple of polysulfide electrolytes (S^{2-}/S_x^{2-}) [34].

As green nanoparticle synthesis remains a challenge, the present study investigated the synthesis and optimization of TiO_2 NPs by newly isolated marine halophilic bacterium *Halomonas* sp. RAM2 and its application in fabricating a novel DSSC using a photosensitizer of carotenoids extracted from the marine bacteria *Kocuria* sp. RAM1. Cu_2S counter electrode was prepared by the SILAR technique and optimized trying to enhance the efficiency, but further study is required to improve the overall conversion efficiency.

Results

Isolation, screening and molecular identification

A salt-tolerant colony was isolated from the sea urchin (*Echinometra mathaei*), collected from Safaga, Red Sea, Egypt. The desirable bacterial isolate was purified and grown on a nutrient agar medium (2% NaCl). Colonies were round, smooth, raised, convex, opaque, and off-white-colored. Microscopic examination revealed that the cells were Gram-negative, non-spore-forming rods. The isolate was referred to as *Halomonas* sp. RAM2 as an outcome of molecular analysis, and the sequence was submitted to GenBank (at the NCBI Nucleotide Database with accession number OM276856) (Fig. 1).

Halomonas sp. RAM2 growth

The physiological characterization of *Halomonas* sp. RAM2 was performed by analyzing salinity tolerance, pH and temperature (Fig. 2). The maximum growth of *Halomonas* sp. RAM2 was observed at 5% NaCl (O.D=1.3) and it tolerated high salinity up to 15% after 33 h. No growth was observed in the absence of NaCl (Fig. 2A). Medium adjusted to pH 8 supported maximum growth (O.D=1.4), whereas pH of 4, 5 and 10 recorded significant low growth (Fig. 2B). Bacterial growth was observed in a range of temperatures (20–37 °C), with maximum growth at 30 °C, while growth inhibition was observed at 40 °C (Fig. 2C).

Biosynthesis and optimization conditions of TiO_2 NPs

The current study deals with extracellular TiO_2 NPs synthesis using cell-free filtrate of *Halomonas* sp. RAM2. The milky-colored suspension confirmed TiO_2 NPs formation, followed by calcination at 500, 600, 700, and 800 °C for further characterization.

TiO_2 concentration (A), pH (B) and reaction time (C) were considered for optimization using response surface methodology (RSM) across 20 runs (Table 1). It was observed that the average size of TiO_2 NPs ranged from 15.45 to 19.48 nm. As per the analysis of variance (ANOVA), the model was statistically significant (p -value=0.0129). Moreover, there was no significant lack of fit for the model, thus suggesting that this model adequately fit the data. Additionally, the determination coefficient ($R^2=0.844$) indicated that the model can explain 84.40% of the variation in the response, indicating the reliability of the model. The predicted R^2 (0.7029) agreed reasonably well with the adjusted R^2 (0.7036). The actual and predicted size averages of TiO_2 NPs are shown in Fig. 3. The final practical model in terms of a coded factor (A = TiO_2 concentration, B = pH, C = time) could be expressed as follows:

$$\begin{aligned} TiO_2 NPs \text{ size (nm)} = & 17.17 - 0.0535 A + 0.8059 B \\ & - 0.5174 C + 0.0831 AB \\ & + 0.0672 AC - 0.2767 BC \\ & + 0.4757 A^2 - 0.0847 B^2 + 0.2962 C^2 \end{aligned} \quad (1)$$

The interaction effect of the three factors on TiO_2 NPs size is demonstrated in Fig. 4. The size of TiO_2 NPs decreased as pH and TiO_2 concentration decreased (Fig. 4A). The smaller size of NPs was also led by the longer duration and lower TiO_2 concentration (Fig. 4B). Thus, the optimal reaction conditions for the smaller TiO_2 NPs size were in the pH range of 5.8–6 with a TiO_2 starting concentration of 0.03 M for 80–102 min.

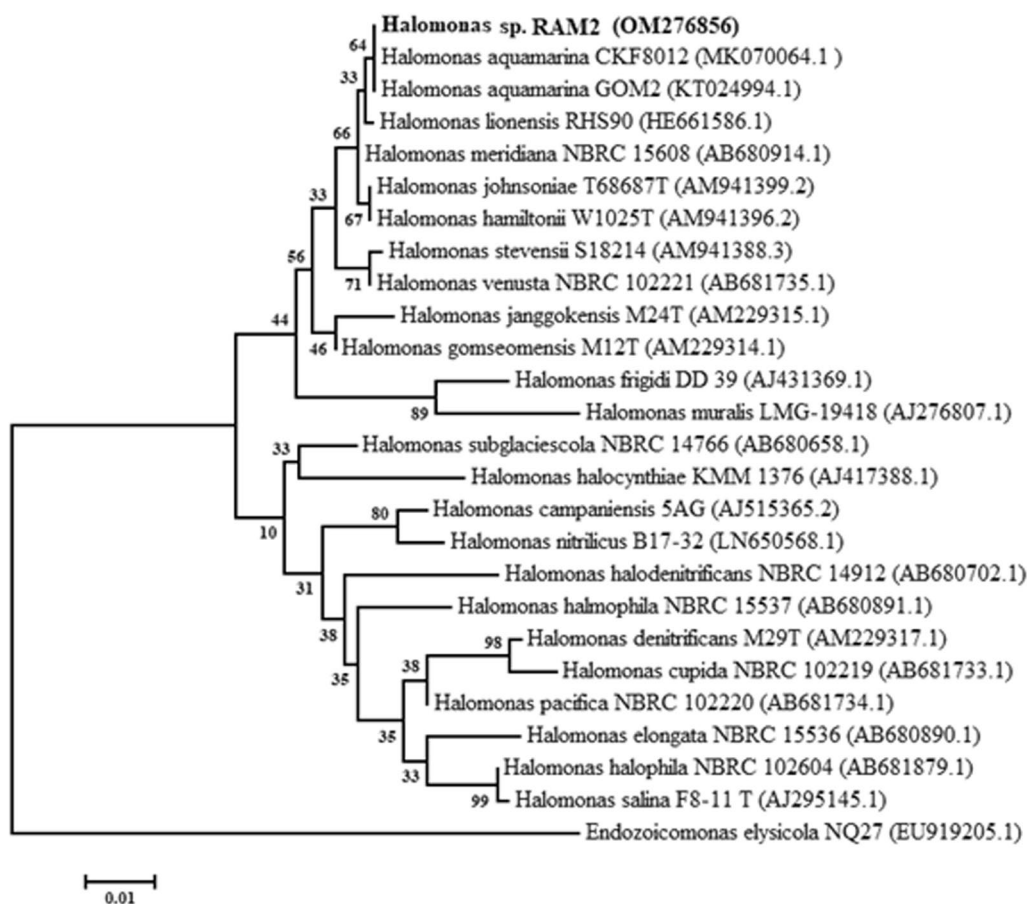


Fig. 1 A phylogenetic tree of *Halomonas* sp. RAM2. The isolate is denoted by a bold style font. GenBank sequence accession numbers are shown in parenthesis after naming the strains

For reaction optimization investigation, the desirability function (DF) was employed. The response value (TiO_2 NP size) was set to a minimum. pH was set to 5, and concentration and time were set within the range for maximum desirability. The starting TiO_2 concentration was 0.031 M, at pH=5 for 92 min. The highest obtained desirability (0.975) was achieved with 15.5 nm TiO_2 NPs. The reaction was validated to confirm the model's adequacy under these predicted optimum conditions, yielding an experimental value of 15.9 nm, which was close to the predicted size (15.5 nm). The comparison that has been made between the predictive and experimental results at the optimum levels indicates that the model has high validity.

Characterization of biogenic TiO_2 NPs

Transmission Electron Microscopy (TEM) Micrographs clearly illustrate the well-defined cubic structure and the variation in size of the biosynthesized TiO_2 NPs after calcination. The size range of samples calcined at 500, 600, 700 and 800 °C was 11–22, 19–26, 29–38 and >80 nm,

respectively (Fig. 5A). It is observed that the uncalcined TiO_2 NPs coagulate while the calcined ones are dispersed uniformly.

The selected area electron diffraction (SAED) Patterns are displayed in Fig. 5B, which shows the crystalline nature of TiO_2 NPs. The intense diffraction rings are indexed as the (101), (004), (200), (211) and (204) planes of the anatase TiO_2 , and the (101), (110) and (211) planes of the rutile TiO_2 .

X-ray diffraction (XRD) is a powerful technique for analyzing NPs crystallinity. A significant shift in the biosynthesized TiO_2 NPs structure was observed after calcination (Fig. 6). Only the anatase TiO_2 phase characteristic peaks (JCPDS 01-089-4921) were well-defined when the sample was calcined at 500 °C, indicating good crystallinity. The peaks indexed to the reflection from (101), (004), (200), (105), (211), (204), (116), (220) and (215) planes at 2θ values of 25.42°, 37.97°, 48.18°, 54.19°, 55.19°, 62.84°, 69.01°, 70.40° and 75.24° correspond to the anatase phase of TiO_2 , respectively. After calcination at 600 °C, new peaks

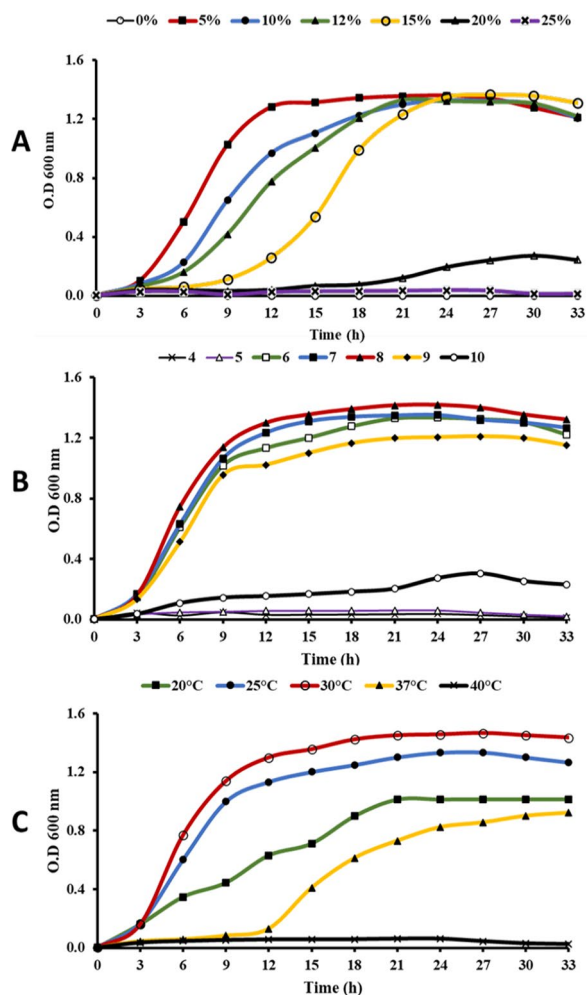


Fig. 2 Growth of *Halomonas* sp. RAM2 in nutrient broth medium at **A** different NaCl concentrations at 30 °C and pH = 7; **B** different pH at 30 °C and 5% NaCl; and **C** different temperatures at pH = 8 and 5% NaCl

corresponding to the rutile phase started to appear in a minor proportion. According to JCPDS 01-089-4920, the peaks at 27.68°, 36.32°, and 41.48° correspond to the (110), (101), and (111) of the rutile phase, respectively. At 700 °C, additional rutile phase peaks (310) and (301) appeared at 2θ of 64.32° and 69.24°, respectively. TiO₂ NPs were completely transformed into the rutile phase with strong peaks at 800 °C, which were clearly represented in (110), (101), (200), (111), (210), (211), (220), (002), (310), (301) and (112) planes.

In terms of size, the temperature affected the size of TiO₂ NPs. NPs calcined at 500 °C were found in the range of 10.16–19.08 nm. And as the temperature was raised to 600 °C, the size of the anatase phase increased from 13.65 up to 27.28 nm, while the new rutile crystal size ranged

Table 1 Experiment design of RSM for 3 operating independent variables affecting TiO₂ NPs size

Run	Reaction conditions			Response	
	A Conc. (M)	B pH	C Time (min)	TiO ₂ Size (nm) Observed	TiO ₂ Size (nm) Predicted
1	0.028	7	90	16.73	17.17
2	0.028	7	90	18.31	17.17
3	0.014	8.2	72	19.48	19.49
4	0.028	7	90	17.88	17.17
5	0.028	7	90	16.87	17.17
6	0.014	8.2	108	17.64	17.77
7	0.028	9	90	18.39	18.28
8	0.028	5	90	15.45	15.57
9	0.005	7	90	18.66	18.60
10	0.041	5.8	108	16.75	16.74
11	0.028	7	120	17.00	17.13
12	0.028	7	60	19.00	18.87
13	0.041	8.2	72	19.22	19.42
14	0.041	8.2	108	18.11	17.96
15	0.041	5.8	72	17.22	17.08
16	0.028	7	90	17.00	17.17
17	0.050	7	90	18.36	18.42
18	0.014	5.8	72	17.35	17.49
19	0.028	7	90	16.20	17.17
20	0.014	5.8	108	17.07	16.88

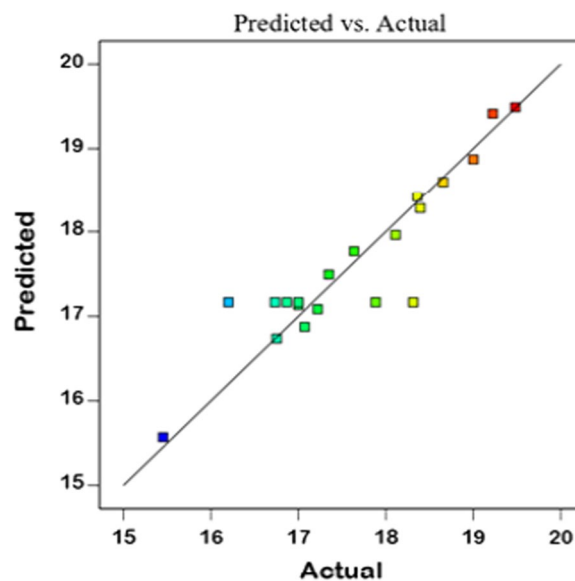


Fig. 3 Actual and predicted plot of TiO₂ NPs size (nm)

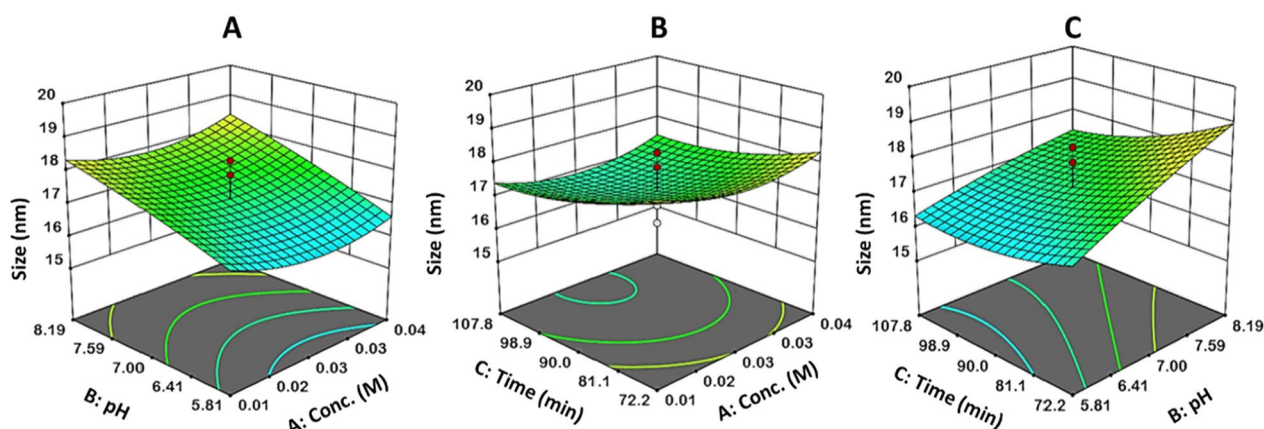


Fig. 4 The 3D surface plots of the interaction effects on TiO₂ NPs size between **A** concentration and pH, **B** concentration and time, and **C** pH and time

from 25 to 28.1 nm. At the anatase–rutile mixed phase of 700 °C, the rutile crystal average size was 30.29 nm, while some of the anatase crystal sizes started to reduce and a larger rutile crystal size was observed at 800 °C. As an outcome, increasing the temperature caused an anatase-to-rutile phase transition, which was characterized by an increase in TiO₂ NPs crystal size.

The optical properties of TiO₂ NPs were investigated in aqueous suspensions (Fig. 7A). Samples calcined at 500 and 600 °C showed almost similar absorption at 300 and 290 nm, respectively, indicating the beginning of the rutile phase with a small proportion. A higher absorption value of 390 nm was obtained at 700 °C, while the absorption of the rutile sample was observed at 250 nm.

The semiconductor band gaps of TiO₂ NPs as determined via the Tauc plots are shown in Fig. 7B. The data were fitted to the indirect band gap for TiO₂ NPs calcined at 500, 600, and 700 °C and were found to be 3.2, 2.6, and 1.6 eV, respectively. The decrease in the band gap energy with increasing calcination temperature indicates anatase to rutile phase transition, as proven by XRD analysis. TiO₂ NPs calcined at 800 °C had a direct band gap of 3.8 eV, indicating a complete rutile phase.

The BET surface area of samples calcined at 500, 600, and 700 °C was 47.96, 37.99, and 26.82 m²/g, respectively (Fig. 8A), while the surface area of the rutile TiO₂ NPs was reduced significantly (9.99 m²/g), indicating the increase in NPs size with temperature. The nitrogen adsorption–desorption isotherm is shown in Fig. 8B. TiO₂ NPs calcined at 500, 600, and 700 °C exhibited a characteristic type IV BET isotherm, indicating their porous nature, while the rutile TiO₂ NPs exhibited a characteristic type III BET isotherm, which explains the lower surface area. The plot of dV (r) vs. pore radius (Fig. 8C) showed a distribution in pore size of 1–25 nm for all samples, with

the high values around 1.6–2.2 nm. The concentrations display a decreasing trend with an increase in pore size in all samples. A sample calcined at 500 °C showed a higher number of pores with diameters of less than 3 nm compared to the other samples calcined at 600, 700, and 800 °C. The pore volumes were determined via the BJH model (Fig. 8D). Samples calcined at 500 and 600 °C exhibited the highest pore volume with slightly similar values (0.18 and 0.17 cc/g, respectively) and an average pore size of 2.28 and 1.68 nm, respectively. A sample calcined at 700 °C exhibited a pore volume of 0.12 cc/g and an average pore size of 1.68 nm, while the rutile TiO₂ NPs exhibited a pore volume of 0.02 cc/g and an average pore size of 1.68 nm.

Energy dispersive X-ray (EDX) of TiO₂ NPs before and after calcination is shown in Fig. 9. The uncalcined TiO₂ sample's major constituents were oxygen (O; 37.75%) and titanium (Ti; 48.15%), in addition to weaker peaks of carbon (C; 5.98%) and nitrogen (N; 7.19%) (Fig. 9A), while the calcined sample showed only oxygen (49.93%) and titanium (50.07%) (Fig. 9B).

NDSSCs performance

The optimum number of SILAR cycles employed in the Cu₂S counter electrode design in NDSSC_{Bio} was 10 cycles [NDSSC_{Bio(10)}], with an efficiency (η) of 0.44%, an open-circuit voltage (V_{OC}) of 213 mV, and a short-circuit current density (I_{sc}) of 1.24E-03 mA/cm², compared to an efficiency (η) of 0.55% resulting from NDSSC_{P25(10)} (Fig. 10). NDSSCs photovoltaic performance is summarized in Table 2.

EIS was recorded at frequencies ranging from 1 Hz to 10 kHz. It aims to analyze and characterize the major internal charge transfer resistances that limit the performance of the cells, which were recorded in the Nyquist

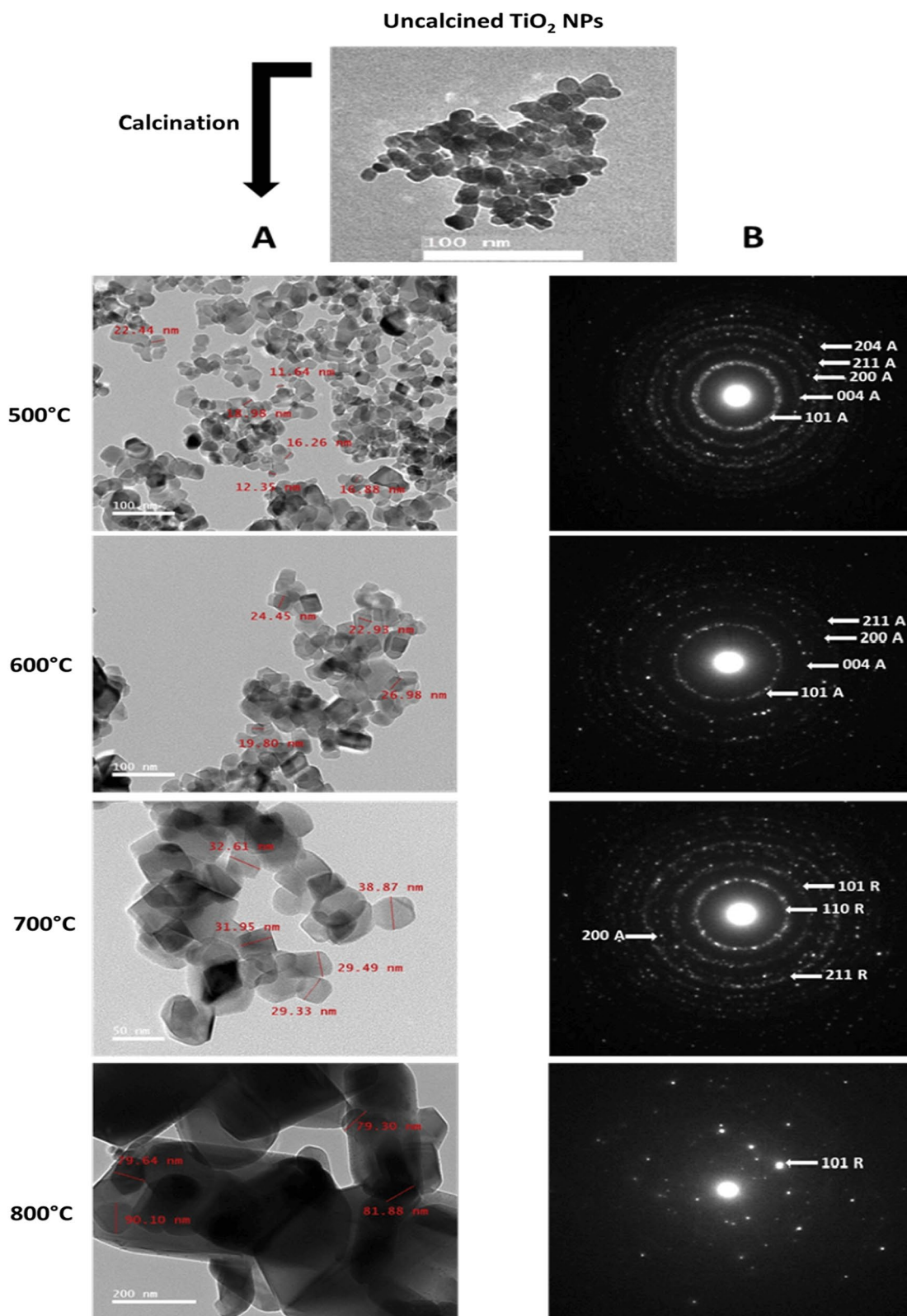


Fig. 5 TEM micrographs of biosynthesized TiO₂ NPs calcined at 500, 600, 700 and 800 °C **A** and the corresponding SAED patterns **B**. A = anatase, R = Rutile

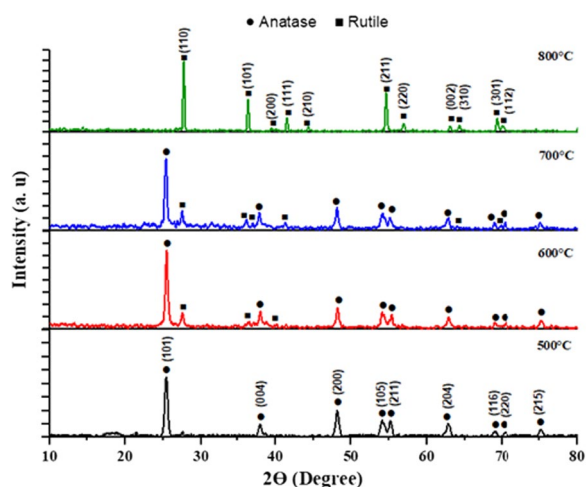


Fig. 6 XRD patterns of biosynthesized TiO_2 NPs calcined at 500, 600, 700 and 800 °C

(Fig. 11A) and Bode plots (Fig. 11B) of the optimized NDSSCs. Well-marked semicircles attributed to the charge transfer resistance between the Cu_2S counter electrode and electrolyte were shown in the high-frequency regions. In the EIS analysis, a smaller diameter of Nyquist plots for the NDSSC_{P25(10)} indicated smaller charge transfer resistance (R_{ct}) than that of the NDSSC_{Bio(10)}, which explained its higher efficiency.

Discussion

Some microorganisms can grow in conditions that most other organisms cannot. Halophiles are one of the most important microbial communities that can tolerate high salt concentrations and are highly sought after by a variety of industries for their unique enzymes and products with broader potential applications [35]. Members of the *Halomonadaceae* family can survive in moderate and Antarctic saline lakes, saline soils, and marine environments regardless of their geographical location. Our work led us to conclude that the starter culture of the *Halomonas* sp. RAM2 strain for TiO_2 NPs synthesis was most preferably performed in a nutrient broth medium supplemented with 5% NaCl, pH = 8, grown at a temperature of 30 °C.

Many microorganisms are capable of producing nanoparticles via either intracellular or extracellular pathways. The current study deals with extracellular TiO_2 NPs synthesis. In terms of application, this has a significant advantage over an intracellular synthesis process because it avoids additional processing steps needed to liberate the nanoparticles from the bacterial cell, either by sonication or by reaction with a suitable detergent [36]. Some studies have shown that TiO_2 NPs with varying crystal sizes were synthesized extracellularly by bacteria such as *Aeromonas hydrophila* (40.5 nm) [37], *Bacillus amyloliquefaciens* (15.23–87.6 nm) [38], *Bacillus licheniformis* (16.3 nm) [39], *Bacillus subtilis* (66–77 nm) [40] and *Lactobacillus* sp. (24.63 nm) [41]. Microorganisms can modify the composition of the solution through the production of extracellular proteins, enzymes, organic polymers and secondary metabolites in the culture

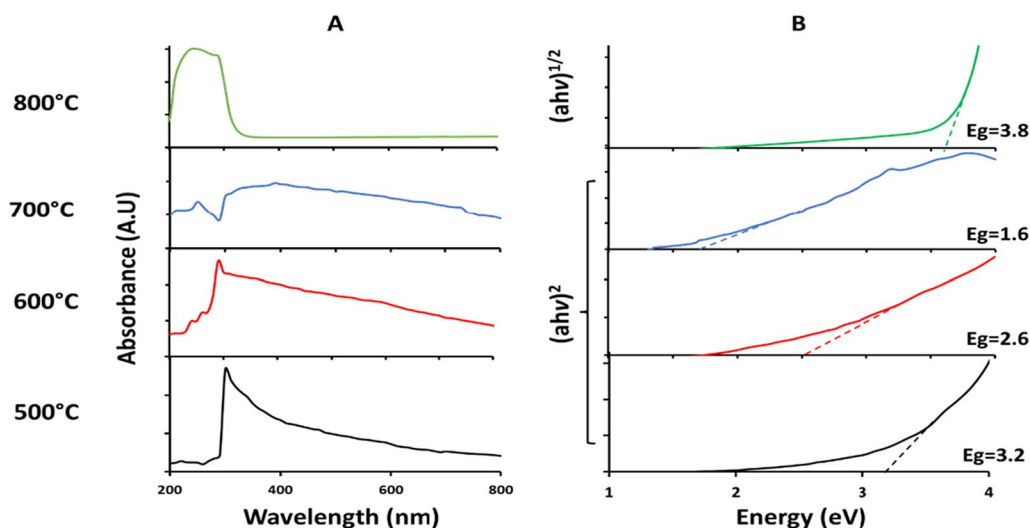


Fig. 7 UV-Vis absorption **A** and the corresponding Tauc plots **B** of *Halomonas* sp. RAM2 TiO_2 NPs calcined at 500, 600, 700 and 800 °C. An Indirect band gap was obtained for TiO_2 NPs calcined at 500, 600 and 700 °C, while a direct band gap was obtained for TiO_2 NPs calcined at 800 °C

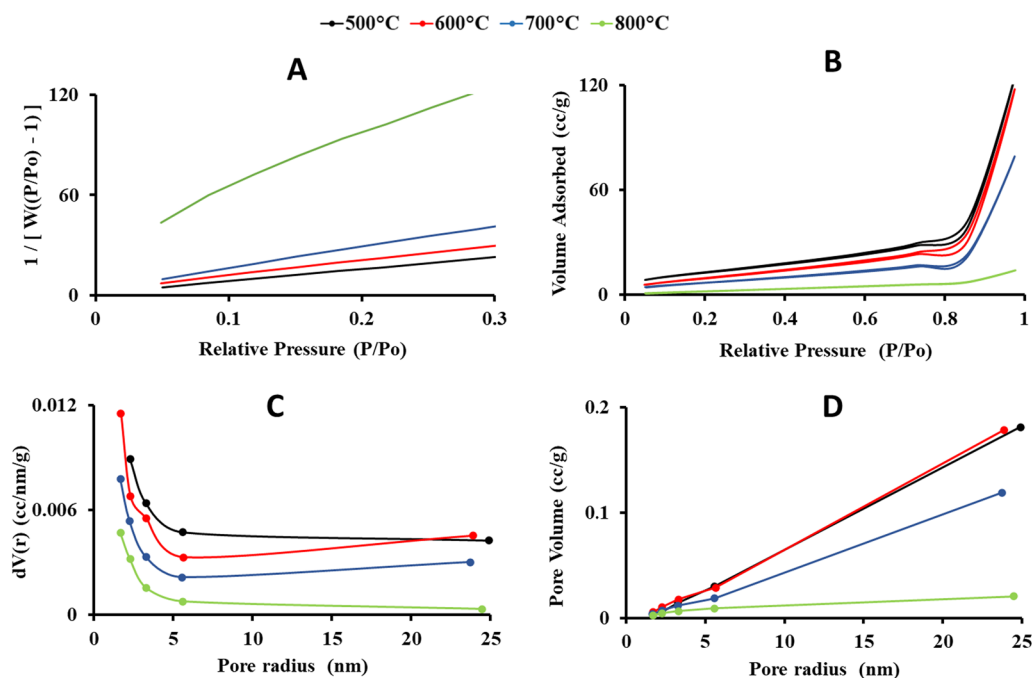


Fig. 8 BET plots **A**, adsorption–desorption isotherms **B**, BJH pore size distribution **C** and cumulative pore volume **D** of *Halomonas* sp. RAM2 TiO₂ NPs calcined at 500, 600, 700 and 800 °C

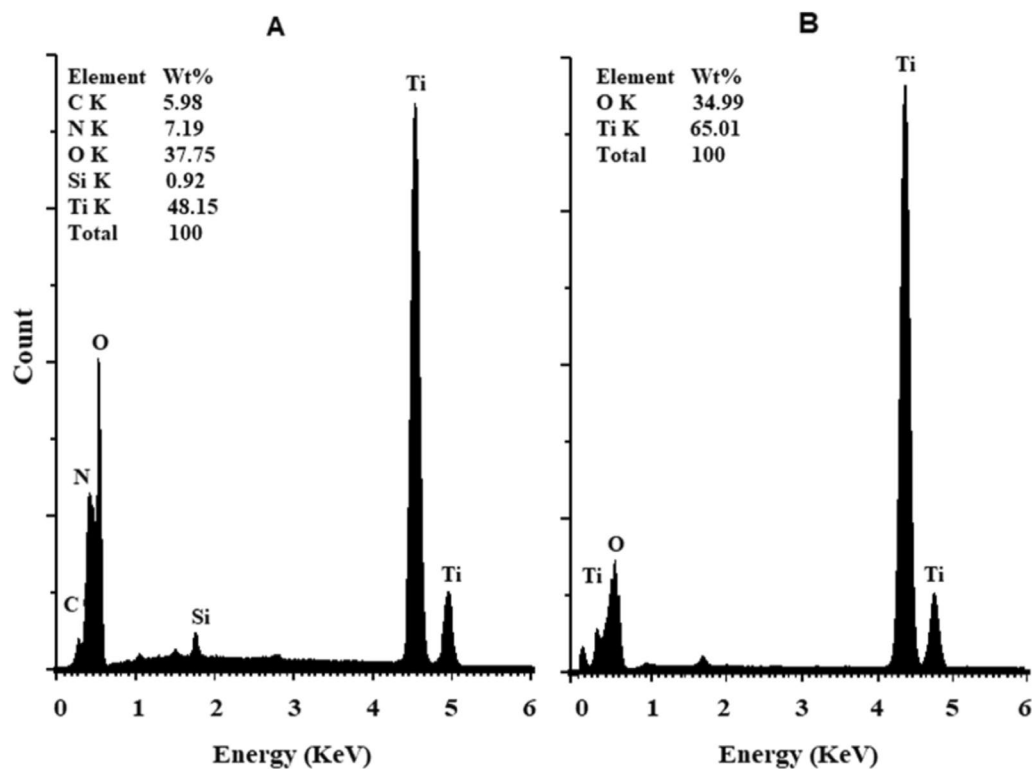


Fig. 9 EDX spectra of uncalcined **A** and calcined **B** samples of biosynthesized TiO₂ NPs

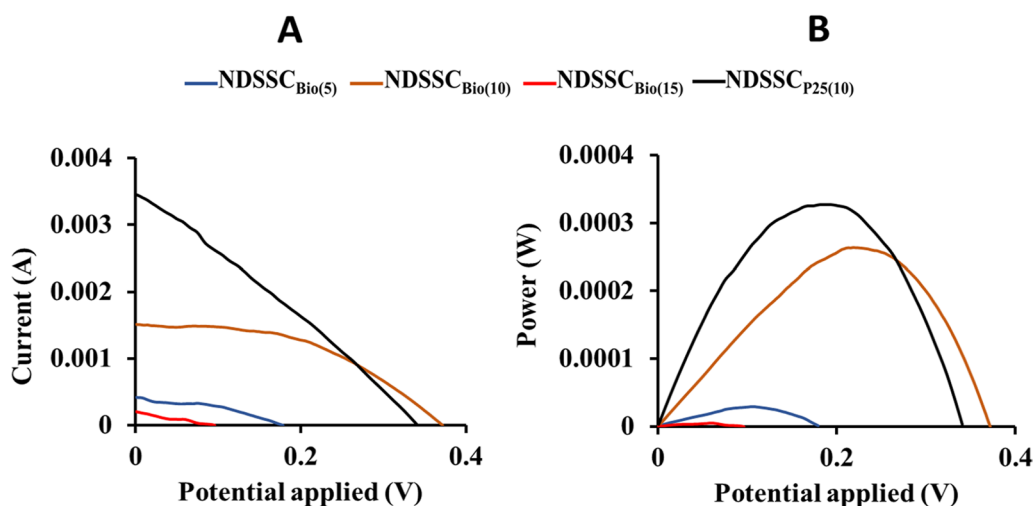


Fig. 10 Photocurrent–voltage characteristics for NDSSC_{Bio} with different counter electrode cycles in comparison to NDSSC_{P25(10)}. **A** J–V characterization. **B** P–V curve

Table 2 Photovoltaic parameters of the NDSSCs

DSSC	V _{oc} (V)	J _{sc} (mA/cm ²)	P _{max}	FF	η (%)
NDSSC _{Bio(5)}	1.06E-01 ± 0.0017	2.72E-04 ± 2.2E-06	2.88E-05 ± 7.8E-07	0.39 ± 0.045	0.048 ± 0.0036
NDSSC _{Bio(10)}	2.13E-01 ± 0.0085	1.24E-03 ± 2.2E-05	2.64E-04 ± 1.1E-05	0.47 ± 0.022	0.44 ± 0.0171
NDSSC _{Bio(15)}	5.95E-02 ± 0.0088	8.92E-05 ± 2.1E-07	5.31E-06 ± 7.8E-08	0.27 ± 0.034	0.0088 ± 0.0002
NDSSC _{P25(10)}	1.84E-01 ± 0.0116	1.78E-03 ± 1.3E-04	3.27E-04 ± 2.3E-05	0.28 ± 0.099	0.55 ± 0.0236

The bold-style efficiency values represent the optimized NDSSCs

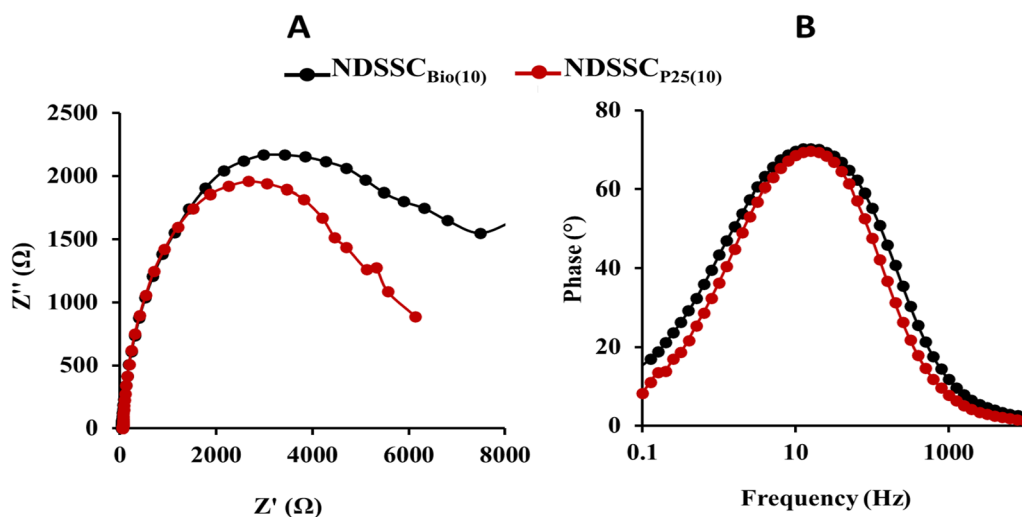


Fig. 11 EIS of the optimized NDSSCs. Nyquist **A** and Bode **B** plots

supernatant, which can influence formation by promoting or hindering the stabilization of the first mineral seeds. So, the metal ions are reduced to nanoparticles [37, 38, 42, 43, 69]. This explains the presence of C and N

in EDX analysis even after several washing steps before calcination at 500 °C.

Controlling particle size is critical in nanoparticle synthesis. In the current study, optimization of reaction

conditions for TiO₂ NPs synthesis has been studied through RSM. One of the most important synthesis parameters was that of the filtrate pH. Some studies proved that pH variation affected the average particle size of TiO₂ NPs, as the lower the pH, the smaller the particle size [44], which indicates that the pH is clearly related to TiO₂ NPs stability. Because each type of NP is stable near the isoelectric point, a change in pH can affect the double-layer properties, boosting the probability of flocculation or coagulation [45, 46]. Previous studies proved that a smaller average size of TiO₂ NPs (14 nm) was obtained at pH=1 in comparison to 19 and 20 nm at pH 7 and 10, respectively [47]. In another study, the average crystallite size varied from 9.92 nm (pH 6.8) to 21.02 nm (pH 5), with the crystallite size decreasing to 7.77 nm in a highly acidic medium (pH 3.2) [48].

From the obtained TEM micrographs and XRD patterns, the conversion of biogenic TiO₂ NPs from anatase to rutile phase began at 700 °C and ended at 800 °C, revealing the formation of a high-temperature stable anatase phase via the green method. This is attributed to the reconstructive action that involves the breaking and reforming of bonds [18]. Heat treatment distorts TiO₆ octahedra during the phase transition. At 700 °C, lattice distortion and breaking of Ti–O bonds affect the removal of oxygen ions, defects, and new Ti–O bond formation. The oxygen vacancies may act as nucleation sites, facilitating the rutile phase formation. The Ti–O bonds are perfectly reconstructed at 800 °C, transition, TiO₂ NPs crystal size increased, leading to a lower surface area [49, 50]. These findings point out that increasing the calcination temperature increases the crystallinity, size, and phase transformation of TiO₂ NPs [51].

By studying the optical properties of the calcined TiO₂ NPs, the band gap was determined. The indirect band gap of TiO₂ decreases with increase of the calcination temperature from 500 °C to 700 °C which is in consistent with previous studies [52]. This might be due to the increase of the particle size and presence of a mixture of the two transition phases of anatase and rutile. The optical band gap of TiO₂ NPs (3.2 eV) calcined at 500 °C was promoted as the most appropriate sample for working electrode fabrication of NDSSCs, as anatase TiO₂ NPs have better photocatalytic activity than rutile TiO₂ NPs in pure phases [53]. The complete conversion to the rutile phase at 800 °C resulted in a direct wider band gap which is attributed to crystal defects formed in the particles.

Our NDSSCs consisted of TiO₂ NPs film, carotenoids, redox polysulfide electrolyte, and a Cu₂S counter electrode. Each component contributes to electron transport and diffusion. TiO₂ acts as a scaffold for dye molecules that have been adsorbed and transports the electrons photogenerated by light absorption and dye regeneration [54]. The interaction between the *Kocuria* sp. RAM1 carotenoids and the TiO₂ NPs resulted from the de-protonation of (-OH) groups of the carotenoids (Fig. 12A), such as bisanhydrobacterioruberin and trisanhydrobacterioruberin. Bacterioruberins are types of C₅₀-carotenoids with a broad absorption range in the visible region (Fig. 12B). They harvest the solar light, leading to being in an excited state, and then inject the photo-excited electrons into the conduction band (CB) of TiO₂ NPs. Because the CB of TiO₂ is at a lower energy level than the lowest occupied molecular orbital (LUMO) of carotenoids, injecting photoelectrons from carotenoids into TiO₂ is energetically advantageous. Through the external circuit, the electrons travel to the counter electrode. The

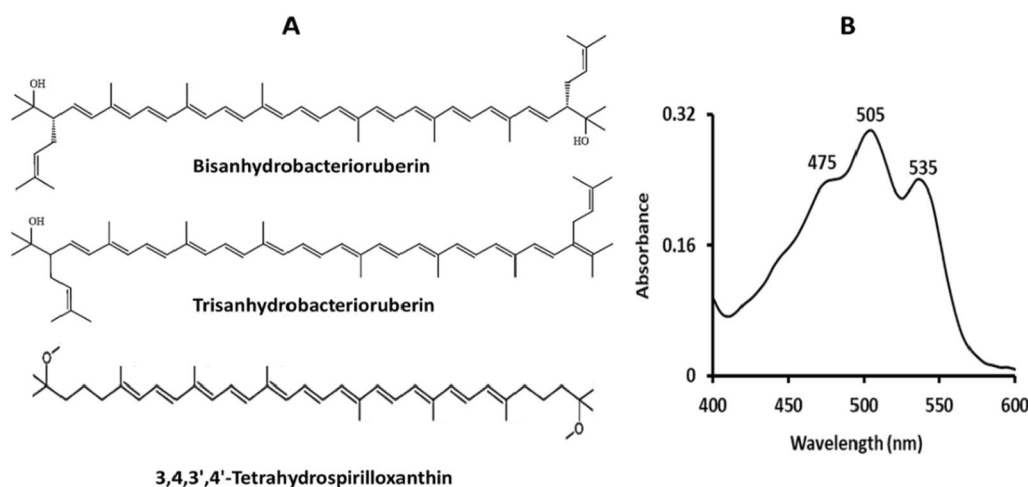


Fig. 12 *Kocuria* sp. RAM1 carotenoids dye composition **A** and UV absorption **B**

oxidized carotenoids accept electrons from the electrolyte, regenerating the ground state [55]. Several studies have reported the utilization of natural dyes extracted specifically from plants in DSSC designs, such as those from pomegranate and berry fruits [56], henna (*Lawsonia inermis*) leaves, beetroot [57], and tropical fruits [58].

Because of its simplicity, low temperature, and uniform layer deposition, the SILAR technique outperforms other methods [59]. A cycle (one layer) of Cu_2S counter electrode film is deposited by the reaction at the substrate surface after the alternative adsorption of Cu^{2+} and S^{2-} ions. The observed optimum NDSSC efficiency was obtained after 10 cycles related to the uniformity, stoichiometry and band gap of the formed Cu_2S film. As previously stated, there is a limited supply of S^{2-} ions from the anionic bath as the number of cycles increases [60].

To the best of our knowledge, this is a novel study that describes the use of C_{50} -carotenoids extracted from marine bacteria as a sensitizer in NDSSCs that involve photo-induced charge transfer into the working electrode of the biosynthesized TiO_2 NPs.

Conclusion

Our study highlighted the eco-friendly TiO_2 biosynthesis by the newly isolated halophilic marine bacteria *Halomonas* sp. RAM2 (OM276856). Also, the study was extended through the application of TiO_2 NPs in NDSSC fabrication using the carotenoids as a natural dye extracted from *Kocuria* sp. RAM1 (OL904955). From an environmental perspective, attempting to fabricate DSSCs using an alternative green method is worthwhile, but further study is required to improve the obtained overall conversion efficiency.

Methods

Isolation, culture medium and identification

Halophilic bacteria were isolated from *Echinodermata* invertebrates collected from Safaga, Red Sea, Egypt. The samples were cut aseptically in sterile seawater, homogenized, and then kept in sterile bottles. One milliliter of each prepared sample was transferred into 100 ml of sterile nutrient broth made with distilled water and supplemented with 2% NaCl (w/v) before being incubated at 30 °C for 24 h under shaking conditions (120 rpm) before being isolated on agar plates for 72 h [61]. The pH was adjusted to 7 ± 0.2 before sterilization. Following incubation, colonies were purified and preserved as stock cultures for subsequent studies. For molecular identification, 16S rDNA was amplified by polymerase chain reaction (PCR) [62]. The PCR products were sequenced [63], and the BLAST program was used to explore the

similarity [64]. The phylogenetic tree was generated using the software MEGA (Version 11.0.10) [65, 66].

NaCl, pH and temperature effects on *Halomonas* sp. RAM2 growth

Bacterial growth (inoculum = 1%) was measured at 120 rpm at various NaCl concentrations (0–25% w/v), pH (5–10) and temperature (20–40 °C). The optical density at a wavelength of 600 nm for 48 h was used as a quantitative indicator [67, 68].

Biosynthesis of TiO_2 NPs using *Halomonas* sp. RAM2

Halomonas sp. RAM2 seed culture was prepared under optimal conditions (NaCl = 5%, pH = 8, 30 °C) at 120 rpm for 48 h (Fig. 13). The culture supernatant was obtained after centrifugation of the broth at 6000 rpm for 15 min and filtrated. After that, the filtrate was challenged with 20 ml of 0.025 M TiO_2 , stirred at room temperature for 1 h, and then heated at 60 °C for 30 min. The biosynthesized TiO_2 NPs were recovered by centrifugation, washed with methanol and distilled water several times, and then dried. The dried sample was calcined at 500, 600, 700, and 800 °C for 3 h for further studies [69].

Optimization of reaction conditions on TiO_2 NPs via response surface methodology (RSM)

The effect of reaction conditions on the TiO_2 NP size via response surface methodology (RSM) through central composite inscribed (CCI) design was investigated using the cell-free filtrate of the *Halomonas* sp. RAM2 optimized growth [70]. Three independent variables using Design Expert (Version 11 Stat-Ease Inc., Minneapolis, MN, USA) were applied to investigate the effects of the starting TiO_2 concentration (A), pH (B) of the cell-free filtrate, and the reaction duration (C) on TiO_2 NPs size (Table 3). The following polynomial equation fits the experimental results:

$$Y = \beta_0 + \beta_1 X_1 + \beta_2 X_2 + \beta_3 X_3 + \beta_{12} X_1 X_2 + \beta_{13} X_1 X_3 + \beta_{23} X_2 X_3 + \beta_{11} X_{11}^2 + \beta_{22} X_{22}^2 + \beta_{33} X_{33}^2 \quad (2)$$

where Y represents the response (TiO_2 NPs size (nm)), β_0 is constant, β_1 , β_2 , and β_3 is linear coefficients, β_{12} , β_{13} , and β_{23} is cross product coefficients, β_{11} , β_{22} , and β_{33} is quadratic coefficients.

The average size of TiO_2 NPs was estimated using XRD analysis and the Scherrer's formula. The model accuracy was determined by the coefficient of R^2 . The *P*-value for the significant model terms was set at 95%.

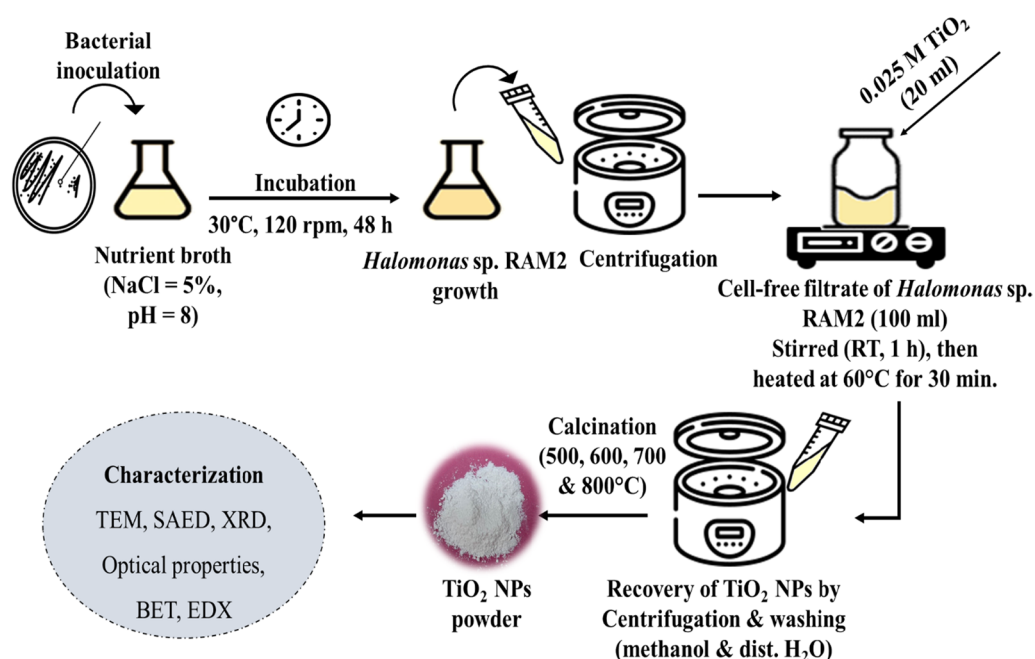


Fig. 13 Schematic diagram of TiO₂ NPs biosynthesis using *Halomonas* sp. RAM2

Table 3 Experimental independent variables and their coded levels for the central composite design

Name	Code	Levels of coded variables				
		−α	−1	0	+1	+α
TiO ₂ concentration (M)	A	0.005	0.0141214	0.0275	0.0408786	0.05
pH	B	5	5.8	7	8.2	9
Reaction duration (min)	C	60	72	90	107	120

Characterization of the biosynthesized TiO₂ NPs

The shape, size and crystallinity of the biogenic TiO₂ NPs were determined by TEM [71] (JEM-2100plus, JEOL, Japan), SAED pattern [72], EDX spectrophotometer [73] and XRD [3]. XRD analysis was performed using an X-ray diffractometer with Cu-Kα crystal radiation ($\lambda = 1.54060 \text{ \AA}$) and scanning rate of ($5^\circ/\text{min}^{-1}$) and the scanning range of ($10^\circ\text{--}80^\circ$). The Scherrer equation was used to calculate the mean diameter of the NPs from the XRD pattern as follows [74]:

$$D = (0.9 \lambda) / (\beta \cos\theta) \quad (3)$$

where $\lambda = 1.5405 \text{ \AA}$ is the wavelength of the Cu-Kα radiation, and β is the full-width at half-maximum (FWHM) intensity in radians.

The TiO₂ NPs optical properties were investigated using a UV/VIS spectrophotometer (Thermo Scientific) in the 200–900 nm wavelength range and the energy band gap was calculated using the Tauc plot (Eq. 4) [75]:

$$(ah\nu)^{(1/n)} = A(h\nu - E_g) \quad (4)$$

where α is the extinction coefficient, h is the Planck's constant (J.S), ν is the light frequency (s^{-1}), A is the absorption constant, E_g is the energy band gap (eV), and n is the value of the specific transition ($n=2$ for indirect band gap and $n=1/2$ for direct band gap).

The Brunauer–Emmett and Teller (BET) (Quantachrome TouchWin v1.2, USA) was used for determination of TiO₂ NPs surface area after degassing the samples at 200 °C for 3 h [76], and Barret–Joyner–Halender (BJH) was used for pore size distribution determination [77].

Fabrication of NDSSCs

Carotenoids as a photosensitizer were extracted from *Kocuria* sp. RAM1 as follows: One liter of a 48-h bacterial culture grown at 30 °C under shaking conditions was centrifuged for 15 min to collect the pellets. 250 ml of methanol were added to the pellet, which was then incubated in a water bath at 40 °C for 15 min until the dye

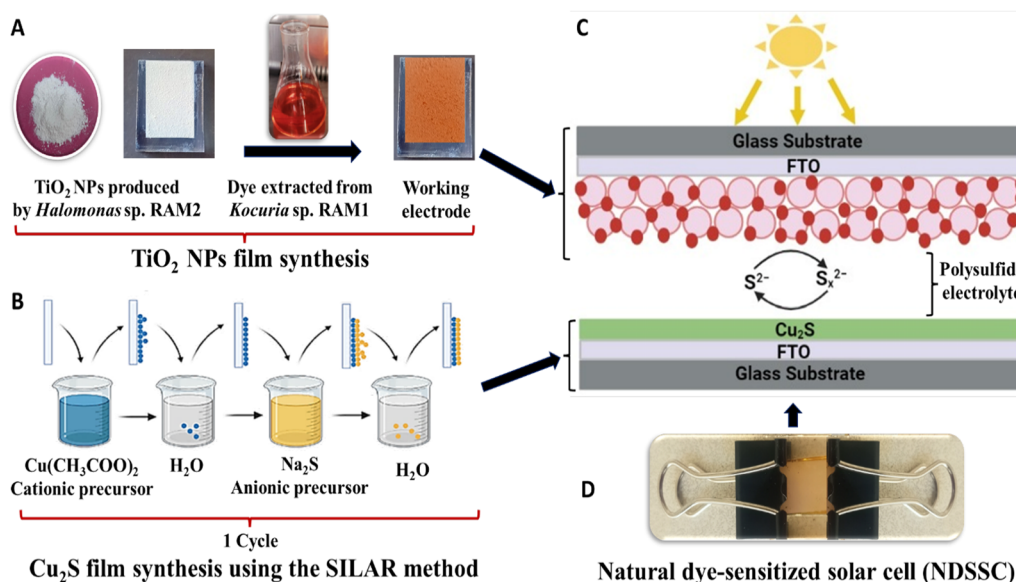


Fig. 14 Illustration of NDSSC fabrication process. **A** Preparation of TiO_2 NPs working electrode. **B** Preparation of Cu_2S counter electrode via the SILAR method. **C** Scheme of NDSSC. **D** Fabricated NDSSC

recovered completely. The extract was purified, dissolved in petroleum ether, and stored in a refrigerator away from direct light [30].

A TiO_2 working electrode was used in the fabricated DSSCs (Fig. 14A). The FTO substrate (15 Ω , Sigma) was cleaned with a detergent solution and successively sonicated for 30 min in soap, then distilled water, then acetone, and finally in isopropanol, respectively, followed by air drying. A TiO_2 paste was made from a mixture of 0.5 g TiO_2 NPs, 1.25 g α -terpineol, 0.25 g ethyl cellulose and a few drops of ethanol. The TiO_2 homogeneous NPs paste was spread over the FTO substrate via a doctor blade coating technique, heated at 450 $^\circ\text{C}$ for 30 min, before being immersed in a concentrated carotenoids dye for 24 h at room temperature [78]. A polysulfide electrolyte solution was prepared from a mixture of 0.5 M Na_2S , 0.1 M S, and 0.05 M KCl in ethanol: water (4:1 vol%) [20].

A Cu_2S counter electrode films were fabricated on an FTO substrate using successive ionic layer adsorption and reaction (SILAR) technique [79]. The cationic precursor was a 0.5 M aqueous solution of copper acetate [$\text{Cu}(\text{CH}_3\text{COO})_2$], while the anionic precursor was 0.5 M of sodium sulfide [Na_2S]. A well-clean FTO-coated glass was immersed in copper acetate for 60 s. to promote ion adsorption on the surface of the substrate, before being immersed in double-distilled water for 20 s. to remove unadsorbed ions. The substrate was then immersed in sodium sulfide for 60 s before the last rinsing step in double-distilled water for 20 s. Thus, one deposition cycle was completed before being annealed in a furnace at 300 $^\circ\text{C}$ for 5 min (Fig. 14B). For optimization, the samples

named NDSSC_{Bio(5)}, NDSSC_{Bio(10)} and NDSSC_{Bio(15)} were prepared by repeating SILAR cycles 5, 10 and 15 times, and the most efficient system was compared to NDSSC equipped with TiO_2 P25 (NDSSC_{P25}) under the same conditions.

The NDSSC was assembled using carotenoid-sensitized TiO_2 coated film that represents the working electrode, Cu_2S film as a counter electrode and the polysulfide electrolyte solution was filled into the cells as illustrated in (Fig. 14C, D).

NDSSCs characterization

The photovoltaic performance [short circuit current (J_{sc}), open circuit voltage (V_{oc}), fill factor (FF), and power conversion efficiency (η)] of the fabricated DSSCs were measured under one sun (AM1.5G, 100 mW/cm^2) illumination using a solar simulator. Electrochemical impedance spectroscopy (EIS) was evaluated using a computer-controlled potentiostat (NOVA 2.0, Metrohm Autolab) under dark conditions [16].

Acknowledgements

The authors are grateful to the National Institute of Oceanography and Fisheries (NIOF), Alexandria, Egypt, the Faculty of Science, Alexandria University, Egypt and Institute of Graduate Studies and Research (IGSR), Alexandria University, Egypt for providing all the facilities to complete this work.

Author contributions

RAM performed the experimental part, prepared all figures, interpreted the data, carried out the analysis and wrote the main manuscript text. JEN helped in solar cells experimental work and contributed to TEM and EDX characterization. SE followed up the solar cells experimental work. NAE and AE assisted with manuscript correction and followed up on the experimental work. SAS followed up the experimental work, revised the manuscript and helped in

manuscript correction. HAG helped in isolate identification and in manuscript correction. All authors read and approved the final manuscript.

Funding

Open access funding provided by The Science, Technology & Innovation Funding Authority (STDF) in cooperation with The Egyptian Knowledge Bank (EKB).

Availability of data and materials

All data generated or analyzed during this study are included in this published article. The datasets of the DNA sequence of the isolated bacterial strains (*Kocuria* sp. RAM1 and *Halomonas* sp. RAM2) analyzed during the current study are available in the GenBank repository under accession numbers OL904955 (<https://www.ncbi.nlm.nih.gov/nucleotide/OL904955>) and OM276856 (<https://www.ncbi.nlm.nih.gov/nucleotide/OM276856.1/>), respectively.

Declarations

Ethics approval and consent to participate

Not applicable.

Consent for publication

All authors consent to the publication of this manuscript.

Competing interests

The authors declare no competing interests.

Author details

¹Marine Microbiology Lab., National Institute of Oceanography and Fisheries, NIOF, Alexandria, Egypt. ²Electronic Materials Department, Advanced Technology and New Materials Research Institute, City of Scientific Research and Technological Applications (SRTA-City), New Borg El-Arab City, Alexandria, Egypt. ³Department of Materials Science, Institute of Graduate Studies and Research, Alexandria University, Alexandria, Egypt. ⁴Marine Pollution Lab., National Institute of Oceanography and Fisheries, NIOF, Alexandria, Egypt. ⁵Botany & Microbiology Department, Faculty of Science, Alexandria University, Alexandria, Egypt.

Received: 13 December 2022 Accepted: 11 April 2023

Published online: 21 April 2023

References

- Chin HS, Cheong KY, Razak KA. Review on oxides of antimony nanoparticles: synthesis, properties, and applications. *J Mater Sci.* 2010;45:5993–6008. <https://doi.org/10.1007/s10853-010-4849-x>.
- Govindaraju K, Basha SK, Kumar VG, Singaravelu G. Silver, gold and bimetallic nanoparticles production using single-cell protein (*Spirulina platensis*) Geitler. *J Mater Sci.* 2008;43:5115–22. <https://doi.org/10.1007/s10853-008-2745-4>.
- Jalali E, Maghsoudi S, Noroozian EA. Novel method for biosynthesis of different polymorphs of TiO₂ nanoparticles as a protector for *Bacillus thuringiensis* from Ultra Violet. *Sci Rep.* 2020;10:426. <https://doi.org/10.1038/s41598-019-57407-6>.
- Algotiml R, Gab-Alla A, Seoudi R, Abulreesh HH, El-Readi MZ, Elbanna K. Anticancer and antimicrobial activity of biosynthesized red sea marine algal silver nanoparticles. *Sci Rep.* 2022;12:2421. <https://doi.org/10.1038/s41598-022-06412-3>.
- Kignelman G, Thielemans W. Meta-analysis of TiO₂ nanoparticle synthesis strategies to assess the impact of key reaction parameters on their crystallinity. *J Mater Sci.* 2021;56:5975–94. <https://doi.org/10.1007/s10853-020-05607-1>.
- Chandren S, Rusli R. Biosynthesis of TiO₂ nanoparticles and their application as catalyst in biodiesel production. In: Nano Green, editor. *Green Nano Solution for Bioenergy Production Enhancement*. Clean Energy Production Technologies. Singapore: Springer; 2022. p. 127–68.
- Thiurunavukkarau R, Shanmugam S, Subramanian K, Pandi P, Muralitharan G, Arokiarajan M, Kasinathan K, Sivaraj A, Kalyanasundaram R, AlOmar SY, Shanmugam V. Silver nanoparticles synthesized from the seaweed *Sargassum polycystum* and screening for their biological potential. *Sci Rep.* 2022;12:14757. <https://doi.org/10.1038/s41598-022-18379-2>.
- Ghorbani HR. Biosynthesis of silver nanoparticles using *Salmonella typhimurium*. *J Nanostruct Chem.* 2013. <https://doi.org/10.1186/2193-8865-3-29>.
- Guan Z, Ying S, Ofoegbu PC, Clubb P, Rico C, He F, Hong J. Green synthesis of nanoparticles: Current developments and limitations. *Environ Technol Innov.* 2022;17:102336. <https://doi.org/10.1016/j.eti.2022.102336>.
- Patil S, Chandrasekaran R. Biogenic nanoparticles: a comprehensive perspective in synthesis, characterization, application and its challenges. *J Genet Eng Biotechnol.* 2020;18:1–23. <https://doi.org/10.1186/s43141-020-00081-3>.
- Bhattarai B, Zaker Y, Bigioni TP. Green synthesis of gold and silver nanoparticles: challenges and opportunities. *Curr Opin Green Sustain Chem.* 2018;12:91–100. <https://doi.org/10.1016/j.cogsc.2018.06.007>.
- Patra JK, Baek KH. Green nanobiotechnology: factors affecting synthesis and characterization techniques. *J Nanomater.* 2014;2014:219. <https://doi.org/10.1155/2014/417305>.
- Lusvardi G, Barani C, Giubertoni F, Paganelli G. Synthesis and characterization of TiO₂ nanoparticles for the reduction of water pollutants. *Materials.* 2017;10:1208. <https://doi.org/10.3390/ma10101208>.
- Poli A, Finore I, Romano I, Gioiello A, Lama L, Nicolaus B. Microbial diversity in extreme marine habitats and their biomolecules. *Microorganisms.* 2017;5:25. <https://doi.org/10.3390/microorganisms5020025>.
- Wang P, Xue M, Jiang D, Yang Y, Zhang J, Dong H, Sun G, Yao Y, Luo W, Zou Z. Photovoltage memory effect in a portable Faradaic junction solar rechargeable device. *Nat Commun.* 2022;13:2544. <https://doi.org/10.1038/s41467-022-30346-z>.
- Yang S, Sha S, Lu H, Wu J, Ma J, Wang D, Sheng Z. Electrodeposition of hierarchical zinc oxide nanostructures on metal meshes as photoanodes for flexible dye-sensitized solar cells. *Coll Surf A Physicochem Eng Asp.* 2020;594:124665. <https://doi.org/10.1016/j.colsurfa.2020.124665>.
- O'Regan B, Grätzel M. A low-cost, high-efficiency solar cell based on dye-sensitized colloidal TiO₂ films. *Nature.* 1991;353:737–40. <https://doi.org/10.1038/353737a0>.
- Hanaor DAH, Sorrell CC. Review of the anatase to rutile phase transformation. *J Mater Sci.* 2011;46:855–74. <https://doi.org/10.1007/s10853-010-5113-0>.
- Su'ait MS, Rahman MYA, Ahmad A. Review on polymer electrolyte in dye-sensitized solar cells (DSSCs). *Sol Energy.* 2015;115:452–70. <https://doi.org/10.1016/j.solener.2015.02.043>.
- Sharma K, Sharma V, Sharma SS. Dye-sensitized solar cells: fundamentals and status. *Nanoscale Res Lett.* 2018;13:381. <https://doi.org/10.1186/s11671-018-2760-6>.
- Satoh N, Nakashima T, Yamamoto K. Metastability of anatase: size dependent and irreversible anatase-rutile phase transition in atomic-level precise titania. *Sci Rep.* 2013;3:1959. <https://doi.org/10.1038/srep01959>.
- Ghasemi S, Hosseini SR, Mousavi F. Electrophoretic deposition of graphene nanosheets: a suitable method for fabrication of silver-graphene counter electrode for dye-sensitized solar cell. *Colloids Surf A Physicochem Eng Asp.* 2017;520:477–87. <https://doi.org/10.1016/j.colsurfa.2017.02.004>.
- Sha S, Lu H, Yang S, Li T, Wu J, Ma J, Wang K, Hou C, Sheng Z, Li Y. One-step electrodeposition of ZnO/graphene composite film as photoanode for dye-sensitized solar cells. *Coll Surf A Physicochem Eng Asp.* 2021;630:127491. <https://doi.org/10.1016/j.colsurfa.2021.127491>.
- Carella A, Borbone F, Centore R. Research progress on photosensitizers for DSSC. *Front Chem.* 2018;6:481. <https://doi.org/10.3389/fchem.2018.00481>.
- Devadiga D, Selvakumar M, Shetty P, Mahesha MG, Devadiga D, Ahipa TN, Kumar SS. Novel photosensitizer for dye-sensitized solar cell based on ionic liquid-doped blend polymer electrolyte. *J Solid State Electrochem.* 2021;25:1461–78. <https://doi.org/10.1007/s10008-021-04920-2>.
- Das SK, Ganguli S, Kabir H, Khandaker JI, Ahmed F. Performance of natural dyes in dye-sensitized solar cell as photosensitizer. *Trans Electr Electron Mater.* 2020;21:105–16. <https://doi.org/10.1007/s42341-019-00158-y>.
- Li L, Furubayashi M, Wang S, Maoka T, Kawai-Noma S, Saito K, Umeno D. Genetically engineered biosynthetic pathways for nonnatural C₆₀ carotenoids using C₅-elongases and C₅₀-cyclases in *Escherichia coli*. *Sci Rep.* 2019;9:2982. <https://doi.org/10.1038/s41598-019-39289-w>.

28. Becker J, Wittmann C. Microbial production of extremolytes—high-value active ingredients for nutrition, health care, and well-being. *Curr Opin Biotech.* 2020;65:118–28. <https://doi.org/10.1016/j.copbio.2020.02.010>.
29. Flegler A, Lipski A. The C₅₀ carotenoid bacterioruberin regulates membrane fluidity in pink-pigmented *Arthrobacter* species. *Arch Microbiol.* 2022;204:70. <https://doi.org/10.1007/s00203-021-02719-3>.
30. Metwally RA, El-Sersy NA, El Sikaily A, Sabry SA, Ghozlan HA. Optimization and multiple in vitro activity potentials of carotenoids from marine *Kocuria* sp RAM1. *Sci Rep.* 2022;12:18203. <https://doi.org/10.1038/s41598-022-22897-4>.
31. Gnanasekar S, Kollu P, Jeong SK, Grace AN. PT-free, low-cost and efficient counter electrode with carbon wrapped VO₂(M) nanofiber for dye-sensitized solar cells. *Sci Rep.* 2019;9:5177. <https://doi.org/10.1038/s41598-019-41693-1>.
32. Zheng W, Zhang S. The effect of CuS counter electrode microtopography on the properties of quantum dot sensitized solar cells. *Inorg Chem Commun.* 2020;122:108294. <https://doi.org/10.1016/j.inoche.2020.108294>.
33. Wu J, Lan Z, Lin J, Huang M, Huang Y, Fan L, Luo G. Electrolytes in dye-sensitized solar cells. *Chem Rev.* 2015;115:2136–73. <https://doi.org/10.1021/cr400675m>.
34. Lee Y-L, Chang C-H. Efficient polysulfide electrolyte for CdS quantum dot-sensitized solar cells. *J Power Sources.* 2008;185:584–8. <https://doi.org/10.1016/j.jpowsour.2008.07.014>.
35. Neelam DK, Agrawal A, Tomer AK, Bandyopadhyaya S, Sharma A, Jagannadham MV, Mandal CC, Dadheech PK. A *Piscibacillus* sp isolated from a soda lake exhibits anticancer activity against breast cancer MDA-MB-231 cells. *Microorganisms.* 2019;7:34. <https://doi.org/10.3390/microorganism7020034>.
36. Bahrulolom H, Nooraei S, Javanshir N, Tarrahimofrad H, Mirbagheri VS, Easton AJ, Ahmadian G. Green synthesis of metal nanoparticles using microorganisms and their application in the agrifood sector. *J Nanobio-technol.* 2021;19:86. <https://doi.org/10.1186/s12951-021-00834-3>.
37. Jayaseelan C, Rahuman AA, Roopan SM, Kirthi AV, Venkatesan J, Kim SK, Iyappan M, Siva C. Biological approach to synthesize TiO₂ nanoparticles using *Aeromonas hydrophila* and its antibacterial activity. *Spectrochim Acta A Mol Biomol Spectrosc.* 2013;107:82–9. <https://doi.org/10.1016/j.saa.2012.12.083>.
38. Khan R, Fulekar MH. Biosynthesis of titanium dioxide nanoparticles using *Bacillus amyloliquefaciens* culture and enhancement of its photocatalytic activity for the degradation of a sulfonated textile dye reactive red 31. *J Colloid Interf Sci.* 2016;475:184–91. <https://doi.org/10.1016/j.jcis.2016.05.001>.
39. Suriyaraj SP, Selvakumar R. Room temperature biosynthesis of crystalline TiO₂ nanoparticles using *Bacillus licheniformis* and studies on the effect of calcination on phase structure and optical properties. *RSC Adv.* 2014;4:39619–24. <https://doi.org/10.1039/C4RA06790H>.
40. Kirthi AV, Rahuman AA, Rajakumar G, Marimuthu S, Santhoshkumar T, Jayaseelan C, Elango G, Zahir AA, Kamaraj C, Bagavan A. Biosynthesis of titanium dioxide nanoparticles using bacterium *Bacillus subtilis*. *Mater Lett.* 2011;65:2745–7. <https://doi.org/10.1016/j.matlet.2011.05.077>.
41. Jha AK, Prasad K, Kulkarni AR. Synthesis of TiO₂ nanoparticles using microorganisms. *Coll Surf B Biointerfaces.* 2009;71:226–9. <https://doi.org/10.1016/j.colsurfb.2009.02.007>.
42. Bansal V, Rautaray D, Bharde A, Ahire K, Sanyal A, Ahmad A, Sastry M. Fungus-mediated biosynthesis of silica and titania particles. *J Mater Chem.* 2005;15:2583–9. <https://doi.org/10.1039/B503008K>.
43. Choi Y, Lee SY. Biosynthesis of inorganic nanomaterials using microbial cells and bacteriophages. *Nat Rev Chem.* 2020;4:638–56. <https://doi.org/10.1038/s41570-020-00221-w>.
44. Zhang H, Chen B, Banfield JF. Particle size and pH effects on nanoparticle dissolution. *J Phys Chem C.* 2010;114:14876–84. <https://doi.org/10.1021/jp1060842>.
45. Gontijo LA, Raphael E, Ferrari DP, Ferrari JL, Lyon JP, Schiavon MA. pH effect on the synthesis of different size silver nanoparticles evaluated by DLS and their size-dependent antimicrobial activity. *Matéria (Rio de Janeiro).* 2020. <https://doi.org/10.1590/S1517-707620200004.1145>.
46. Suttiponparmit K, Jiang J, Sahu M, Suvachittanont S, Charinpanitkul T, Biswas P. Role of surface area, primary particle size, and crystal phase on titanium dioxide nanoparticle dispersion properties. *Nanoscale Res Lett.* 2011. <https://doi.org/10.1007/s11671-010-9772-1>.
47. Sadiq SA, Waseem Z, Hanif S, Riaz S, Hayat K, Batool AI, Jamil Y, Naz MY, Anwar H. Investigation of the role of pH on structural and morphological properties of titanium dioxide nanoparticles. *IOP Conf Ser Mater Sci Eng.* 2020;863:012046. <https://doi.org/10.1088/1757-899X/863/1/012046>.
48. Tsega M, Dejene FB. Influence of acidic pH on the formulation of TiO₂ nanocrystalline powders with enhanced photoluminescence property. *Heliyon.* 2017;3:e00246. <https://doi.org/10.1016/j.heliyon.2017.e00246>.
49. Choudhury B, Choudhury A. Local structure modification and phase transformation of TiO₂ nanoparticles initiated by oxygen defects, grain size, and annealing temperature. *Int Nano Lett.* 2013;3:55. <https://doi.org/10.1186/2228-5326-3-55>.
50. Wetchakun N, Incessungvorn B, Wetchakun K, Phanichphant S. Influence of calcination temperature on anatase to rutile phase transformation in TiO₂ nanoparticles synthesized by the modified sol–gel method. *Mater Lett.* 2012;82:195–8. <https://doi.org/10.1016/j.matlet.2012.05.092>.
51. Kim MG, Kang JM, Lee JE, Kim KS, Kim KH, Cho M, Lee SG. Effects of calcination temperature on the phase composition, photocatalytic degradation, and virucidal activities of TiO₂ nanoparticles. *ACS Omega.* 2021;6(16):10668–78. <https://doi.org/10.1021/acsomega.1c00043>.
52. Lal M, Sharma P, Ram C. Calcination temperature effect on titanium oxide (TiO₂) nanoparticles synthesis. *Optik.* 2021;241:166934. <https://doi.org/10.1016/j.jijleo.2021.166934>.
53. Luttrell T, Halpegamage S, Tao J, Kramer A, Sutter E, Batzill M. Why is anatase a better photocatalyst than rutile?—Model studies on epitaxial TiO₂ films. *Sci rep.* 2014;4:4043. <https://doi.org/10.1038/srep04043>.
54. González-Verjan VA, Trujillo-Navarrete B, Félix-Navarro RM, de León JN, Romo-Herrera JM, Calva-Yáñez JC, Hernández-Lizalde JM, Reynoso-Soto EA. Effect of TiO₂ particle and pore size on DSSC efficiency. *Mater Renew Sustain Energy.* 2020;9:13. <https://doi.org/10.1007/s40243-020-00173-7>.
55. Amogne NY, Ayele DW, Tsigie YA. Recent advances in anthocyanin dyes extracted from plants for dye sensitized solar cell. *Mater Renew Sustain Energy.* 2020;9:23. <https://doi.org/10.1007/s40243-020-00183-5>.
56. Ghann W, Kang H, Sheikh T, Yadav S, Chavez-Gil T, Nesbitt F, Uddin J. Fabrication, optimization and characterization of natural dye sensitized solar cell. *Sci Rep.* 2017;7:41470. <https://doi.org/10.1038/srep41470>.
57. Sathyajothi S, Jayavel R, Dhanmozhi AC. The fabrication of natural dye sensitized solar cell (DSSC) based on TiO₂ using henna and beetroot dye extracts. *Mater Today Proc.* 2017;4:668–76. <https://doi.org/10.1016/j.matpr.2017.01.071>.
58. Murrillo E, Giuffrida D, Menchaca D, Dugo P, Torre G, Meléndez-Martínez AJ, Mondello L. Native carotenoids composition of some tropical fruits. *Food Chem.* 2013;140:825–36. <https://doi.org/10.1016/j.foodchem.2012.11.014>.
59. Mali SS, Shinde PS, Betty CA, Bhosale PN, Oh YW, Patil PS. Synthesis and characterization of Cu₂ZnSnS₄ thin films by SILAR method. *J Phys Chem Solids.* 2012;73:735–40. <https://doi.org/10.1016/j.jpics.2012.01.008>.
60. Banu NN, Ravichandran K. Analysis of sulphur deficiency defect prevalent in SILAR-CdS films. *J Mater Sci: Mater Electron.* 2017;28:11584–90. <https://doi.org/10.1007/s10854-017-6959-6>.
61. Makridis P, Kokou F, Bournakas C, Papandroulakis N, Sarropoulou E. Isolation of *Phaeobacter* sp. from larvae of Atlantic bonito (*Sarda sarda*) in a mesocosms unit, and its use for the rearing of European seabass larvae (*Dicentrarchus labrax* L.). *Microorganisms.* 2021. <https://doi.org/10.3390/microorganisms9010128>.
62. Lane DJ. 16S/23S rRNA sequencing. In: Stackenbradt E, Goodfellow M, editors. *Nucleic Acid Techniques in Bacterial Systematics.* New York: John Wiley and Sons; 1991. p. 177–203.
63. Dinzouna-Boutamba SD, Yang HW, Joo SY, Jeong S, Na BK, Inoue N, Lee WK, Kong HH, Chung DI, Goo YK, Hong Y. The development of loop-mediated isothermal amplification targeting alpha-tubulin DNA for the rapid detection of *Plasmodium vivax*. *Malaria J.* 2014;13:248. <https://doi.org/10.1186/1475-2875-13-248>.
64. Johnson M, Zaretskaya I, Raytselis Y, Merezukh Y, McGinnis S, Madden TL. NCBI blast: a better web interface. *Nucleic Acids Res.* 2008;36:W5–9. <https://doi.org/10.1093/nar/gkn201>.
65. Kumar S, Stecher G, Tamura K. Mega7: molecular evolutionary genetics analysis version 70 for bigger datasets. *Mol Biol Evol.* 2016;33:1870–4. <https://doi.org/10.1093/molbev/msw054>.
66. Tamura K, Stecher G, Kumar S. Mega11: molecular evolutionary genetics analysis version 11. *Mol Biol Evol.* 2021;38:3022–7. <https://doi.org/10.1093/molbev/msab120>.

67. Das P, Chatterjee S, Behera BK, Dangar TK, Das BK, Mohapatra T. Isolation and characterization of marine bacteria from east coast of india: functional screening for salt stress tolerance. *Heliyon*. 2019;5:e01869. <https://doi.org/10.1016/j.heliyon.2019.e01869>.
68. Li F, Xiong XS, Yang YY, Wang JJ, Wang MM, Tang JW, Liu QH, Wang L, Gu B. Effects of NaCl concentrations on growth patterns, phenotypes associated with virulence, and energy metabolism in *Escherichia coli* BW25113. *Front Microbiol*. 2021;12:705326. <https://doi.org/10.3389/fmicb.2021.705326>.
69. Sunkar S, Nachiyar CV, Lerencha R, Renugadevi K. Biogenesis of TiO₂ nanoparticles using endophytic *Bacillus cereus*. *J Nanopart Res*. 2014;16:2681. <https://doi.org/10.1007/s11051-014-2681-y>.
70. Box GE, Wilson KB. On the experimental attainment of optimum conditions. *J Roy Stat Soc B Met*. 1951;13:1–45. <https://doi.org/10.1111/j.2517-6161.1951.tb00067.x>.
71. Lee B, Yoon S, Lee JW, Kim Y, Chang J, Yun J, Ro JC, Lee JS, Lee JH. Statistical characterization of the morphologies of nanoparticles through machine learning based electron microscopy image analysis. *ACS Nano*. 2020;14:17125–33. <https://doi.org/10.1021/acsnano.0c06809>.
72. Mali SS, Kim H, Shim CS, Patil PS, Kim JH, Hong CK. Surfactant free most probable TiO₂ nanostructures via hydrothermal and its dye sensitized solar cell properties. *Sci Rep*. 2013;3:3004. <https://doi.org/10.1038/srep03004>.
73. Noman MT, Petru M, Amor N, Yang T, Mansoor T. Thermophysiological comfort of sonochemically synthesized nano TiO₂ coated woven fabrics. *Sci Rep*. 2020;10:17204. <https://doi.org/10.1038/s41598-020-74357-6>.
74. Scherrer P. Bestimmung der inneren struktur und der Größe von Kolloidteilchen Mittels Röntgenstrahlen. *Kolloidchemie Ein Lehrbuch*. 1912. https://doi.org/10.1007/978-3-662-33915-2_7.
75. Tauc J, Grigobovici R, Vancu A. Optical properties and electronic structure of amorphous germanium. *Phys Status Solidi (b)*. 1966;15:627–37. <https://doi.org/10.1002/pssb.19660150224>.
76. Brunauer S, Emmett PH, Teller E. Adsorption of gases in multimolecular layers. *J Am Chem Soc*. 1938;60:309–19. <https://doi.org/10.1021/ja01269a023>.
77. Barrett EP, Joyner LG, Halenda pp. The determination of pore volume and area distributions in porous substances. I. computations from nitrogen isotherms. *J Am Chem Soc*. 1951;73:373–80. <https://doi.org/10.1021/ja01145a126>.
78. Shaikh S, Mane R, Min B, Hwang YJ, O-shim Joo. D-sorbitol-induced phase control of TiO₂ nanoparticles and its application for dye-sensitized solar cells. *Sci Rep*. 2016;6:20103. <https://doi.org/10.1038/srep20103>.
79. Salaramoli H, Maleki E, Shariatinia Z, Ranjbar M. CDs/CdSe quantum dots co-sensitized solar cells with Cu₂S counter electrode prepared by SILAR, spray pyrolysis and Zn–Cu Alloy Method. *J Photoch Photobio A Chem*. 2013;271:56–64. <https://doi.org/10.1016/j.jphotochem.2013.08.006>.

Publisher's Note

Springer Nature remains neutral with regard to jurisdictional claims in published maps and institutional affiliations.

Ready to submit your research? Choose BMC and benefit from:

- fast, convenient online submission
- thorough peer review by experienced researchers in your field
- rapid publication on acceptance
- support for research data, including large and complex data types
- gold Open Access which fosters wider collaboration and increased citations
- maximum visibility for your research: over 100M website views per year

At BMC, research is always in progress.

Learn more biomedcentral.com/submissions

